crystals

MDPI

Article

Effects of Sintering Processes on Microstructure Evolution, Crystallite, and Grain Growth of MoO_2 Powder

Jongbeom Lee [1,*], Jinyoung Jeong [1,2], Hyowon Lee [3], Jaesoung Park [3], Jinman Jang [1] and Haguk Jeong [1]

[1] Industrial Materials Processing R&D Group, Korea Institute of Industrial Technology, Incheon 21999, Republic of Korea; zero5677@kitech.re.kr (J.J.); man4502@kitech.re.kr (J.J.); hgjeong@kitech.re.kr (H.J.)
[2] Department of Advanced Materials Science and Engineering, Inha University, Incheon 22212, Republic of Korea
[3] Thin Film Materials R&D Team, LT Metal. Co., Ltd., Incheon 21697, Republic of Korea; hwlee@ltmetal.co.kr (H.L.); jaspark@ltmetal.co.kr (J.P.)
* Correspondence: ljb01@kitech.re.kr; Tel.: +82-32-850-0378

Abstract: MoO_2 micro-powders with a mean pore size of 3.4 nm and specific surface area of 2.5 g/cm^3 were compacted by dry pressing, then pressureless sintered at a temperature of 1000–1150 °C for 2 h or for a sintering time of 0.5–12 h at 1050 °C in an N_2 atmosphere. Then, their microstructure evolution for morphology, crystallite, and grain growth were investigated. By sintering at a certain temperature and times, the irregular shape of the MoO_2 powders transformed into an equiaxed structure, owing to the surface energy, which contributed to faster grain growth at the initial stage of sintering. The crystallite and grain sizes exponentially increased with the sintering time, and the growth exponent, n, was approximately 2.8 and 4, respectively. This indicates that the crystallite growth is governed by dislocation-mediated lattice diffusion, and the grain growth is determined by surface diffusion-controlled pore mobility. The increase in sintering temperature increased both crystallite and grain size, which obeyed the Arrhenius equation, and the activation energies were determined to be 95.65 and 76.95 kJmol^{-1} for crystallite and grain growths, respectively.

Keywords: MoO_2; sintering; XRD; SEM; morphology; crystallite; grain growth

Citation: Lee, J.; Jeong, J.; Lee, H.; Park, J.; Jang, J.; Jeong, H. Effects of Sintering Processes on Microstructure Evolution, Crystallite, and Grain Growth of MoO_2 Powder. *Crystals* **2023**, *13*, 1311. https://doi.org/10.3390/cryst13091311

Academic Editor: Andreas Thissen

Received: 5 August 2023
Revised: 23 August 2023
Accepted: 26 August 2023
Published: 28 August 2023

1. Introduction

Molybdenum oxides, a type of metal oxide with an *n*-type semiconducting and non-toxic nature, have attracted much attention for their diverse functional applications such as electronics, catalysis, sensors, energy-storage units, field emission devices, superconductor lubricants , thermal materials, biosystems, and chromogenic and electrochromic systems [1–3]. MoO_X ($2 \leq X \leq 3$) has a high work function of approximately 6.7 eV and can be used as the hole-extraction layer in photovoltaic devices, light-emitting devices, and sensors, owing to its photochromism and low reflectance characteristics [4,5].

MoO_X not only has many intermediate oxides such as Mo_nO_{3n-1} between MoO_2 and MoO_3, but also has various structural and electronic phases due to the multiple valence states of 4d molybdenum from +3 to +6 [6,7]. Among them, the most common are MoO_3 and MoO_2, which differ in their electronic and optical properties and chemical structures. MoO_3 has an orthorhombic structure and consists of two layers of MoO_6 octahedra as a framework [8]. MoO_2 has a disfigured rutile structure, which consists of MoO_6 octahedra coupled by edge-sharing [9]. Regarding the optical properties, MoO_3 usually presents as white, whereas MoO_2 exhibits as dark blue or black, allowing a different light absorption characteristic [10]. MoO_2 is electrically conductive, but MoO_3 is insulating [11,12]. This metallic property of MoO_2 endows it with possible applications as electrodes for gas sensors and catalysis [13–15].

MoO_2 is less important in technological applications than MoO_3 but has been used as a catalyst for alkane isomerization or oxidation reactions and as a gas sensor. Furthermore, MoO_2 is an oxide-based compound semiconductor with an indirect band gap, and it is also a potential candidate for desirable hole injection layer applications between a transparent conducting oxide (TCO) and an organic light-emitting diode (OLED) [16]. For the fine bezel in a thin-film transistor (TFT) backplane, MoO_2 can be applied as a functional film to lower the reflection of a metal-mesh electrode and enhance the effect of shadow elimination; additionally, it is a cost-effective and reliable thin-film material [17].

MoO_2 thin films can be fabricated using a molybdenum target using spin coating, pulsed laser deposition, reactive sputtering, and thermal evaporation [18]. In the case of the sputtering process, to optimize the performances of the thin film, most researchers have studied the influences of sputtering parameters on the film properties, including the type of sputter power (radio-frequency (RF) magnetron reactive sputtering, direct current (DC) magnetron reactive sputtering), working pressure (oxygen partial pressure from 1.00×10^{-3} mbar to 1.37×10^{-3} mbar), base pressure, atmosphere (Ar-O_2 sputtering gas), sputter powder (electrical conductivity varying from 1.6×10^{-5} S/cm to 3.22 S/cm), film thickness, and post-annealing treatment (oxygen annealing range from 250 to 350 °C) [19–23]. However, it is difficult to elucidate how the target influences the properties of various films, the sputtering process, and the correlations between film properties and target performance have not been well established. Therefore, recently, sputtering targets have gradually grown in importance because the sintered density, grain size, electrical properties, stoichiometry, and microstructural uniformity of the sputtering targets are now known to significantly influence not only the properties of various thin films but also the sputtering process. Understanding and controlling a sputtering target's crystallite and grain growth is important in thin film deposition processes, as it can affect the quality and properties of the deposited thin film [24].

The use of MoO_2 materials instead of Mo materials makes the optimization of process parameters easier because MoO_2 thin film is fabricated by reactive sputtering of Mo target materials in a controlled O_2 atmosphere. Several works [25–27] have investigated the fabrications and microstructural evolution of Mo materials by powder metallurgy, but studies on a fabrication of bulk materials using MoO_2 powders by means of the sintering process and its microstructural evolution during firing are limited. Therefore, this study systematically investigated commercially available MoO_2 powders to determine the effects of the sintering temperature and time on microstructure evolution for the morphology of the powder, grain growth. MoO_2 bulk materials were fabricated from MoO_2 powder using a conventional sintering process at different sintering temperatures and times. The crystalline structure, powder morphology, and microstructural evolution of the sintered MoO_2 were characterized via X-ray diffraction (XRD) and scanning electron microscopy (SEM). Moreover, the kinetics and activation energy for crystallite and grain growths were determined and elucidated based on lattice and surface diffusion mechanisms, respectively.

2. Materials and Methods

The as-received MoO_2 powders had irregular polygonal structures (Figure 1a), particle sizes with a mean diameter of 2.1 μm (Figure 1b), and a purity of 99.9%. The powders were compacted into a cylindrical shape with a diameter of 6 mm and thickness of 3 mm at a uniaxial press by applying 200 MPa at ambient temperature, and after pressure application the time of 10 min is provided for even spreading of pressure. The compacted samples were dried at 120 °C in an oven for 2 h before sintering. The MoO_2 sample was sintered at 1000–1150 °C for 2 h, and at 1050 °C for 0–12 h in an N_2 atmosphere. A constant heating rate of 5 °C/min and a dwell time of 2 h was applied at various temperatures. To assure specific temperature control, a type-B thermocouple (Thermo Fisher Scientific, Waltham, MA, USA) was applied in the furnace equipment, and the electric power obligated for the set sintering schedule was traced down using the potentiometer.

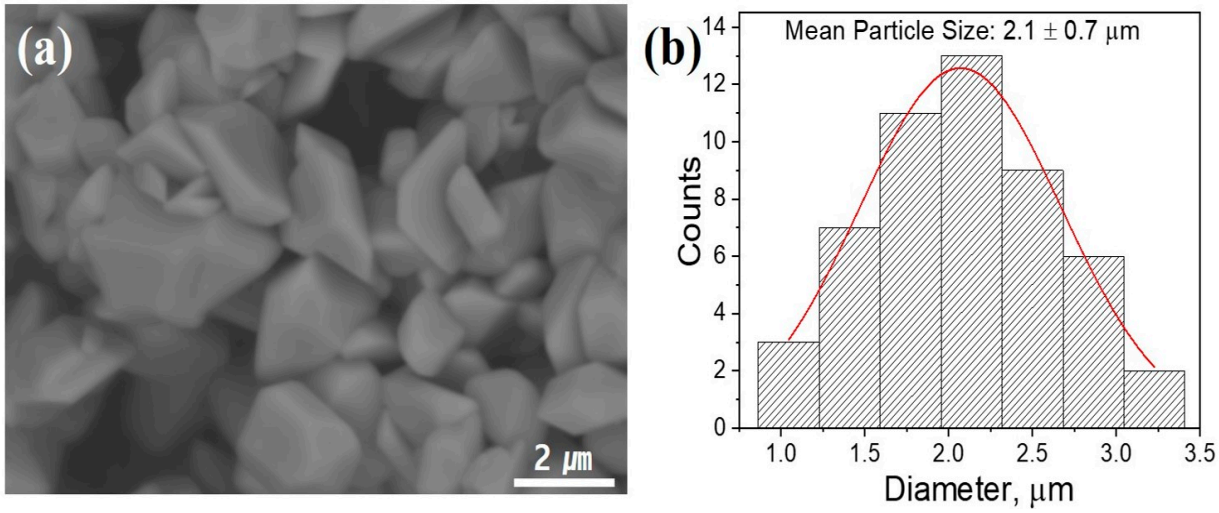

Figure 1. (**a**) SEM photo and (**b**) histogram demonstrating the particle size distribution of the as-received MoO_2 powders.

The specific surface area (SSA) and pore size of the MoO_2 micro-powders were determined using an automatic adsorption instrument (Quanta chrome Corp. Quadrasorb evo, Boynton Beach, FL, USA). Sample degassing was performed at 170 °C for 13 h, before the absorption and desorption of liquid N_2 at –196 °C (77 K). The MicroActive 4.0 software (TriStar II 3020 version 2.0) was used to generate the Brunauer–Emmett–Teller (BET) surface area and the Barrett–Joyner–Helenda (BJH) pore size distribution. The sintered samples were identified using X-ray diffractometry (XRD, Smartlab, Rigaku Co.,Tokyo, Japan) to determine the lattice parameters and dislocation density (Cu Kα, λ = 1.54059 Å, 25 mA × 40 kV power, in the range of 2θ = 20–80°, and a step size of 0.02°) at room temperature. The XRD results were obtained using the software for the powerful Rietveld refinement method (Crystal Impact GbR, Bonn, Germany). Highscore Plus files from CrystalMaker software version 10.8.2. were used to generate a crystal structure of the sintered sample. The morphology and microstructure of the powders and the fractured surface of the sintered samples were investigated by SEM at an accelerating voltage of 20 kV (SU5000, Hitachi, Tokyo, Japan). To impede the specimen charging, a layer of platinum was coated onto the powder and sintered samples for 15 s. The particle and grain sizes of the powders and sintered samples were measured using image analysis software (Image-Pro, Media Cybernetics Inc., Rockville, MD, USA).

3. Results and Discussion

The BET isotherms for nitrogen adsorption by the as-received MoO_2 powders were measured to evaluate the pore structure. As shown in Figure 2a, the distinctive hysteresis loop was mainly observed at a higher pressure, i.e., P/P_0 = 0.0–1.0, indicating a type IV isotherm, which is indicative of a typical mesoporous material [28]. The hysteresis loop is formed because of the difference in the capillary action in the mesopores and macropores during the absorption and desorption process [29]. The pore size distribution, determined from the adsorption–desorption curve using the BJH method, was analyzed as a function of the pore diameter of the MoO_2 powders, as shown in Figure 2b, which shows the pore size distribution for pore diameters ranging from 1 to 300 nm. The SSA of the powders determined from the N_2 adsorption–desorption isotherm using the BET method was 2.5 m^2g^{-1}, macropores of size larger than 50 nm rarely existed, and the mean pore size was approximately 3.4 nm (Figure 2b).

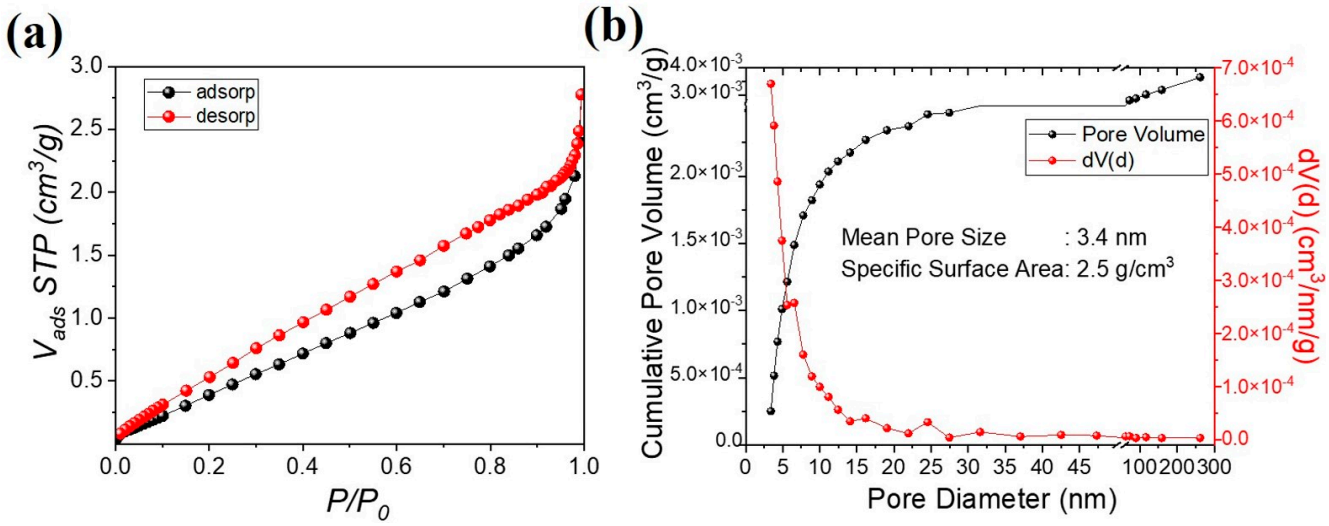

Figure 2. (**a**) N_2 adsorption-desorption isotherms and (**b**) cumulative pore volume and BJH pore size distribution curves of as-received MoO_2 powders.

XRD patterns and crystal structure modeling of the as-received and sintered samples are shown in Figure 3. The XRD results exhibit characteristic peaks, similar to a previous study [30], and the as-received powders have a monoclinic structure with a lattice parameter of a = 5.6102 Å, b = 4.8573 Å, c = 5.6265 Å, and β = 120.915°, showing crystal structure modeling (Figure 3b). The dashed lines in Figure 3a indicate the peak of the main *hkl* miller indices of the as-received and sintered samples, indicating that each lattice parameter is invariant under the sintering process in this study, while the phase transition of MoO_2 from monoclinic structure to a tetragonal structure at T = 1260 °C (1533 K) was reported in a previous study [31].

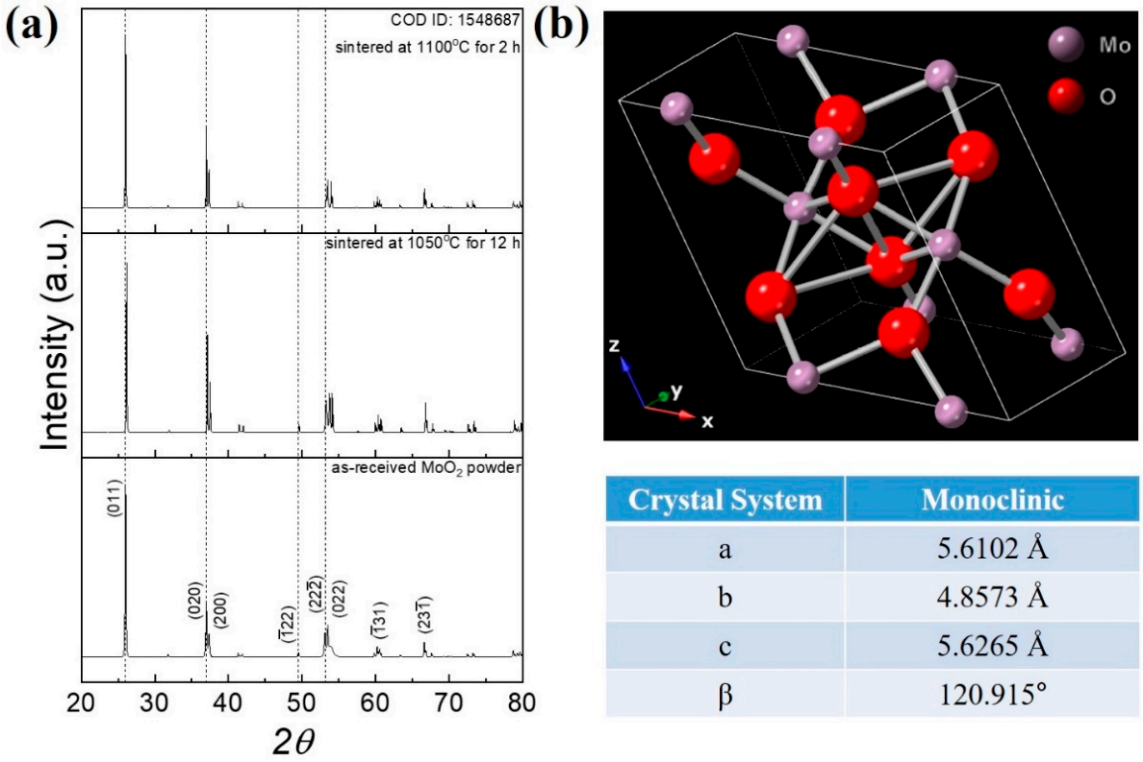

Crystal System	Monoclinic
a	5.6102 Å
b	4.8573 Å
c	5.6265 Å
β	120.915°

Figure 3. (**a**) XRD patterns and (**b**) crystal structure modeling and lattice parameters of the as-received and sintered samples.

The microstructures of the fracture cross-section of the sintered samples at different times and histograms of the grain size distribution are shown in Figure 4. By increasing the sintering time at 1050 °C, the as-received MoO_2 particles transformed from an irregular polygonal structure (Figure 1a) to those with a regular geometry with a nearly spherical structure (Figure 4c,d). After elapsing the sintering time of 2 h at 1050 °C, roughly rounded grains were roughly found in small and large grains, suggesting that a concave surface acts to pull itself into a flat surface to decrease the surface energy. Subsequently, the presence of surface tension forces induced by the difference in the curvature of the powder, which tends to minimize the surface area of materials, can cause the material to adopt a more rounded shape. The histograms of the grain size distribution of the sintered samples at different times show that the grains grow with increasing sintering time, and finally, the mean grain size reached 4.7 μm and the standard deviation of the grain sizes slightly increased. Grain growth refers to a particle's volume change by grain boundary motion and its driving force is proportional to the mean of curvature on the grain boundary. The convex grain boundaries of smaller particles move inward, and smaller particles shrink. Therefore, as the sintering time increases, the standard deviation of the grain sizes increases because the radius of the curved grain boundary reduces when smaller particle shrinks [32].

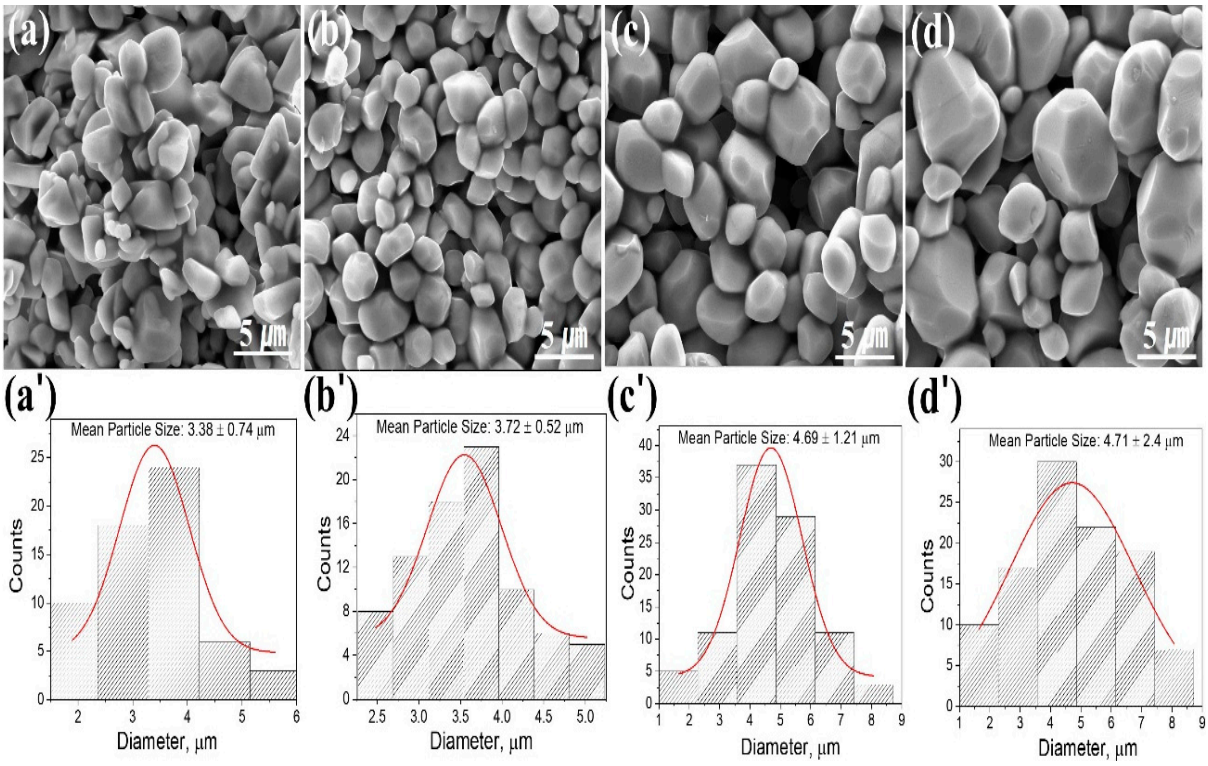

Figure 4. SEM photographs of the fracture cross-section of the sintered MoO_2 sample at 1050 °C for (**a**) 0.5, (**b**) 2, (**c**) 6, (**d**) 12 h; (**a'**–**d'**) show the histograms of grain size distribution.

Figure 5 shows the microstructures and grain size variation in the sintered samples' fracture cross-sections with increasing sintering temperatures for 2 h. Similar to Figure 4, the as-received MoO_2 powder with an irregular polygonal structure exhibits a partially further spherical shape when the sintering temperature was increased above 1000 °C, owing to the generation of surface tension force, capillary action, and particle rearrangement, as previously mentioned. Unlike Figure 4, particles with a partially spherical shape were observed in Figure 5a at a lower sintering temperature of 1000 °C for 2 h, indicating that the transformation from the irregular polygonal structure to a rounded shape is caused by sintering for sufficient time as well as over the temperature. By increasing the sintering temperature, the grain size distribution increased, as shown in Figure 5a'–d'. Higher

sintering temperatures provide more thermal energy for grain boundary migration and coalescence, resulting in larger grain sizes and an increase in grain size distribution.

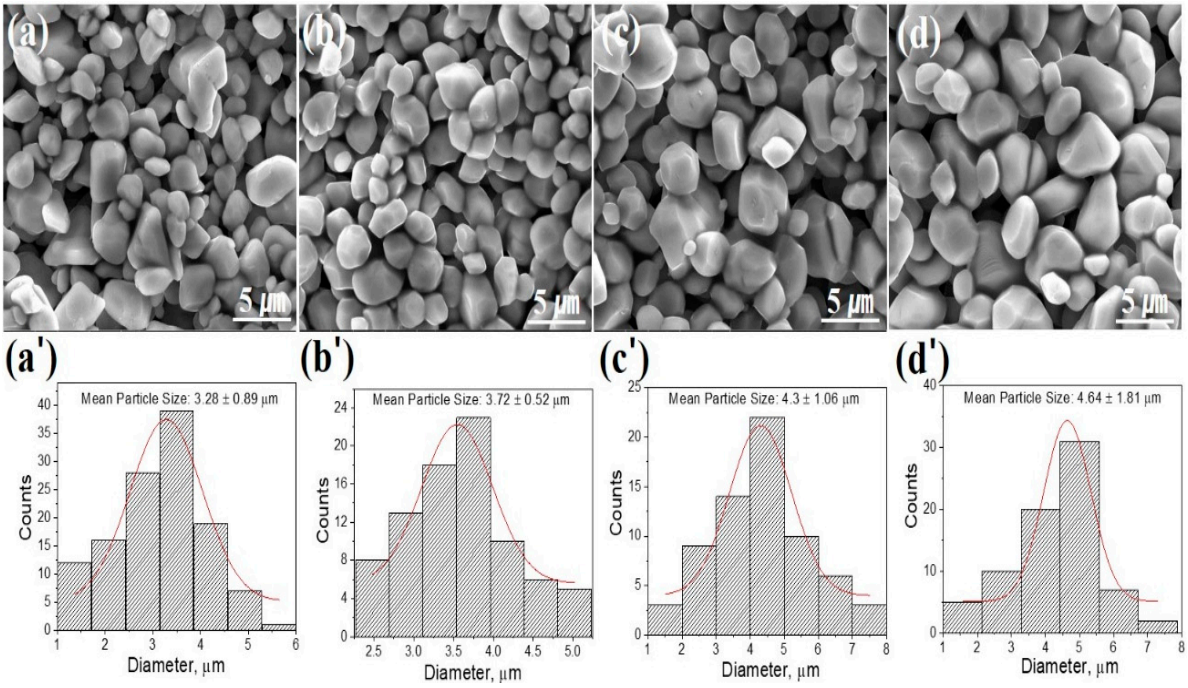

Figure 5. SEM photographs of fracture cross-section of sintered MoO_2 sample depending on different temperatures of (**a**) 1000, (**b**) 1050, (**c**) 1100, (**d**) 1150 °C for 2 h; (**a′**–**d′**) show the histograms of grain size distribution.

Based on the XRD patterns (Figure 2a), the crystallite size was calculated using the Scherrer equation, which considers the broadening of a peak in a diffraction pattern to relate the size of sub-micrometer crystallites as follows [33,34]:

$$D_{hkl} = \frac{C\lambda}{B_{hkl} \cdot cos\theta}, \delta = 1/D_{hkl}^2 \quad (1)$$

where D_{hkl} is the crystallite size in the direction perpendicular to the lattice planes, C is a numerical factor frequently referred to as the crystallite-shape factor and $C = 0.9$ is a good approximation [35], λ is the wavelength of the X-rays, B_{hkl} is the width (full-width at half-maximum) of the XRD peak in radians, θ is the Bragg angle, and δ is the dislocation density. Figure 6a,b show the variation in mean crystallite sizes and dislocation density, obtained from the Scherrer equation, according to the annealing time and temperature, respectively. Based on the obtained graph, the mean crystallite size increased, and dislocation density decreased with the sintering time and temperature. As shown in Figure 6a, crystallite growth was rapid in the initial stage and gradual after the intermediate stage. During the initial stages of heating, the crystallite growth rate increases rapidly, and concurrently the dislocation density decreases swiftly. However, as the crystallites increase in size, they begin to hinder crystallite growth owing to the decrease in dislocation density; thus, the growth rate decreased. Eventually, the growth rate decreased until the decrease rate in dislocation density was effectively negligible. As shown in Figure 6b, the growth of the mean crystallite size depends on the sintering temperature, and it was correlated with the variation in the dislocation density. At the same sintering time of 2 h, the mean crystallite size increased linearly with the decrease in dislocation density, indicating that the crystallite growth is correlated with the variation in the dislocation density. Dos Reis et al. [36] also show that the dislocation plays as an effective fast diffusivity channel in MgO based on kinetic Monte Carlo simulations testified by atomistic calculations.

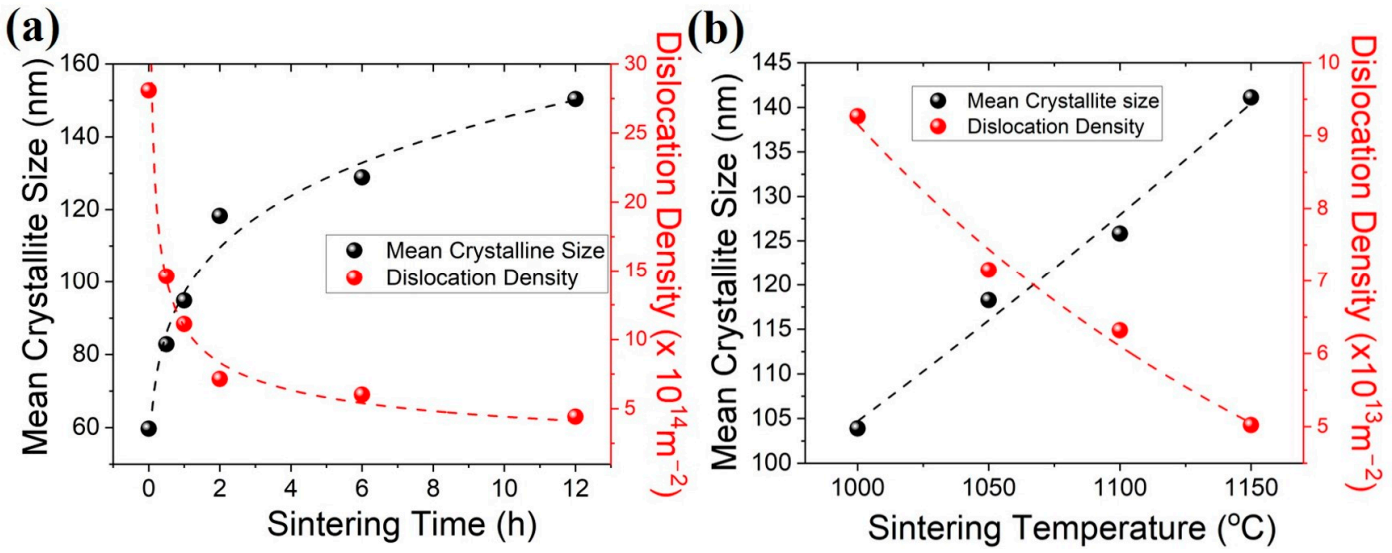

Figure 6. Evolution of the mean crystallite size and dislocation density of the samples as a function of (**a**) various holding times at a sintering temperature of 1050 °C and (**b**) various sintering temperatures for 2 h.

Figure 7 shows the variation in the average grain size of sintered samples with various sintering times at 1050 °C and various sintering temperatures for 2 h. As shown in Figure 7a, the average grain size sharply increased for the sintering time of 2 h, and then steadily increased until 12 h at the same sintering temperature. The graph shows that the grain growth rate is very high in the first 0.5 to 2 h, and then the growth rate decreases. Grain growth processes are also related to the mechanisms of grain boundary motion; thus, it is assumed that the instantaneous rate of growth is directly proportional to the instantaneous average rate of grain boundary migration in the structure, calculated as [37]

$$\frac{d\overline{G}}{dt} \sim \overline{v} \tag{2}$$

where $\overline{G}$ is the average grain size and $\overline{v}$ is the velocity of grain boundary motion. A grain boundary proceeds with a velocity ($\overline{v}$) in response to the net pressure on the boundary. It is generally given that the velocity is directly proportional to the pressure, with the constant of proportionality being the grain boundary mobility (M), and thus,

$$\overline{v} = MP \tag{3}$$

The driving force for boundary movement in ceramics is mostly acquired from the pressure gradient ΔP across the boundary arising from its curvature, given by [38]

$$\Delta P = S\left(\frac{1}{r_1} + \frac{1}{r_2}\right) = S\left(\frac{1}{K\overline{G}}\right) \tag{4}$$

where S is the grain boundary energy, r_1, and r_2 are the two radii of curvature of the boundary surface, and K is a constant. The pressure gradient ΔP decreases as the mean grain size $\overline{G}$ increases as a function of sintering time. Consequently, the reduction in ΔP could also contribute to the decrease in the velocity of grain boundary motion at the intermediate and final steps of the sintering process. By increasing the sintering temperature, grain coarsening occurs because higher temperatures provide more thermal energy for grain boundary movement and coalescence, resulting in larger grain sizes.

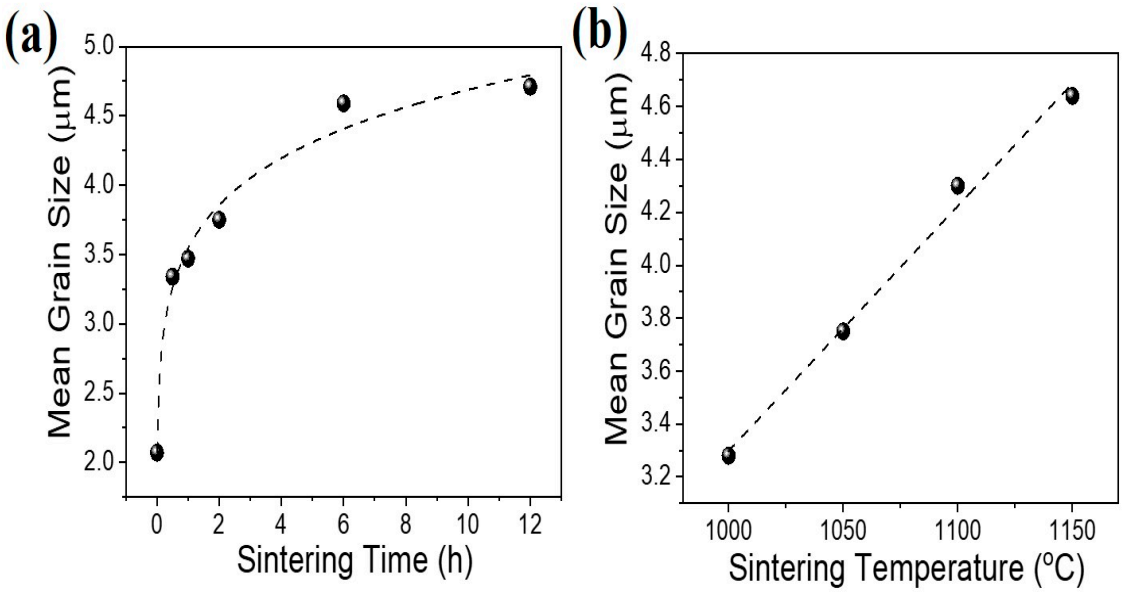

Figure 7. Changes in the mean grain size of the samples as a function of (**a**) various holding times at a sintering temperature of 1050 °C and (**b**) various sintering temperatures for 2 h.

Using the data on the crystallite and grain size variation with the sintering processes (Figures 6 and 7), the kinetic and activation energy of grain growth can be evaluated as shown in Figure 7. The grain (or crystallite) growth can be calculated as follows [39].

$$G - G_0 = K' t^{1/n} \quad (5)$$

where G is the mean grain size, G_0 is the initial grain size, K' is a temperature-dependent constant, t is the time, and n is the grain growth exponent representing the grain growth behavior. Here, D on the left of the Y-axis of Figure 7a is the mean crystallite size. The n value can be calculated using the data analysis software of Origin (Origin Lab, Northampton, MA, USA) using an allometric equation (y = aχˆb). Figure 7a shows that the m values for crystallite and grain growth are approximately 2.8 and 4, respectively. According to the literature [38], the values of the grain growth exponent n have been determined in the kinetics of grain growth for various mechanisms: n values of lattice and surface diffusion for pore-controlled systems are 3 and 4, respectively, and n = 2 for the boundary-controlled system. In this study, it is reasonable to assume that the n value of 2.8 for crystallite growth is mainly controlled by the lattice diffusion, and that of 4 for grain growth is predominantly governed by surface diffusion for pore-controlled systems. The activation energy (Q) of grain growth can be obtained by [39]

$$K' = K'_0 \exp\left(-\frac{Q}{RT}\right) \quad (6)$$

where Q is the activation energy, T is the temperature in Kelvin, K'_0 is the pre-exponential rate constant, and R is the gas constant. This explains why a plot of $ln(G - G_0)$ vs. $1/T$ produces a straight line (Figure 8b). The crystallite and grain growth activation energies are 95.62 and 76.96 kJ/mol, respectively. The grain growth representing the exponent n with a value of approximately 4 is the system where pore mobility is controlled by surface diffusion [38]. The activation energy of the grain growth should indicate the activation energy of the pore mobility controlled by surface diffusion in the sintered MoO_2 samples. On the contrary, an exponent of $n \approx 3$ describes the activation energy governed by lattice diffusion. Based on the interpretation, the value of the calculated activation energy of the crystallite and grain growth could be accepted given that crystallite growth is controlled by lattice diffusion through a dislocation channel, and grain growth is governed by surface diffusion of a pore mobility. Then, the value of activation energy for crystallite growth is greater than that for grain growth. However, it is difficult to identify a grain growth

mechanism based on the exponent n alone, because Ganapathi et al. [29] obtained excellent fits for all values of n = 2, 3, or 4 with different annealing temperatures and times based on measurements on nanocrystalline Cu. Nevertheless, it is notable that the comparison between the kinetics and activation energies for the crystallite and grain growth could reliably be evaluated by the large reduction of some intrinsic limitations because of the same experimental conditions, namely, model parameters, acquisition temperature and time, purity, and usage of the same materials.

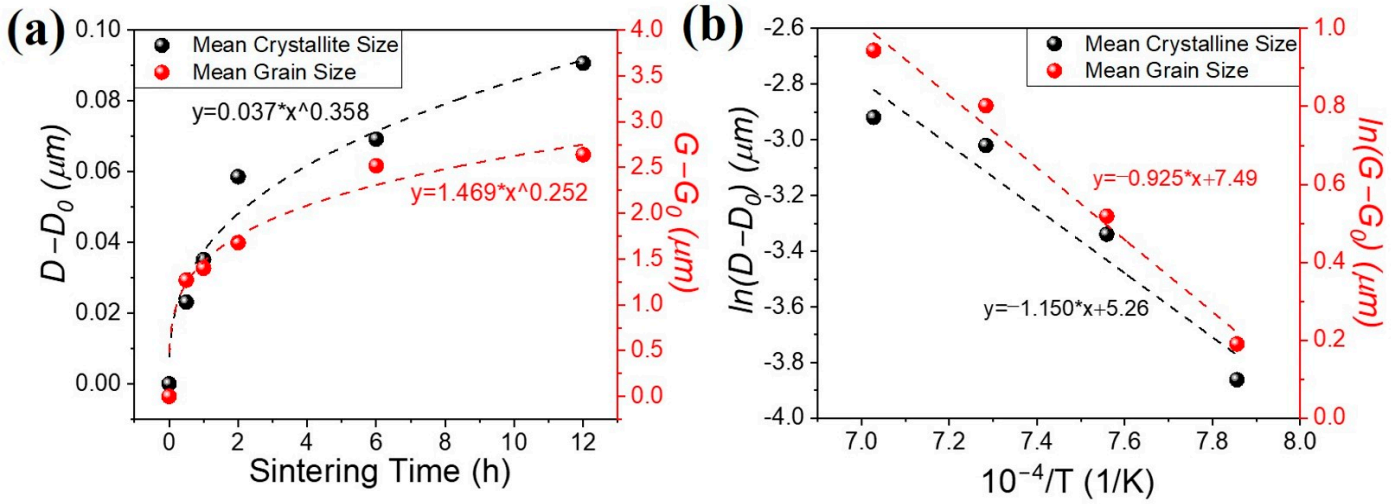

Figure 8. Variation of (**a**) $D - D_0$ and $G - G_0$ with different sintering times at 1050 °C and (**b**) plots of $In(D - D_0)$ and $ln(G - G_0)$ vs. $1/T$ for different sintering temperatures at the durations of 2 h.

4. Conclusions

Compacted MoO_2 powders by dray pressing were sintered at various temperatures and times in an N_2 atmosphere, and their microstructure evolution was characterized using XRD and SEM images. As the sintering process reached a certain temperature and time, the irregular shape of as-received MoO_2 powders transformed into an equiaxed structure, owing to the occurrence of surface tension force, following which, the grain started to grow to decrease the surface energy. In accord with the Scherrer equation based on the XRD pattern, the crystallite size increased gradually as the sintering time and temperature increased, and the variation in grain size with sintering processes exhibited analogous trends as the change in the crystallite size. The crystallite and grain size exponentially increased with a growth exponent, n, of approximately 2.8 and 4, respectively, indicating that the growth kinetic can be governed by dislocation-mediated lattice diffusion and surface diffusion-controlled pore mobility, respectively. With increasing sintering temperature, both crystallite and grain size obeyed the Arrhenius equation against $1/T$, and the activation energies were 95.65 and 76.95 kJmol^{-1}, respectively.

Author Contributions: Conceptualization, J.L. and J.J. (Jinyoung Jeong); methodology, J.J. (Jinyoung Jeong), H.J. and J.J. (Jinman Jang); software, J.L.; validation, J.L.; formal analysis, J.J. (Jinyoung Jeong); investigation, J.J. (Jinyoung Jeong) and J.J. (Jinman Jang); resources, H.L. and J.P.; data curation, J.J. (Jinman Jang); writing—review and editing, J.L.; supervision, H.L. and J.P.; project administration, H.L. and J.P.; funding acquisition, J.P. All authors have read and agreed to the published version of the manuscript.

Funding: This research was funded by the Ministry of Trade, Industry and Energy, grant number 20022463, Korea.

Data Availability Statement: Not applicable.

Conflicts of Interest: The authors declare no conflict of interest.

References

1. De Castro, I.; Datta, R.; Ou, J.; Castellanos-Gomez, A.; Sriram, S.; Daeneke, T.; Kalantar-Zadeh, K. Molybdenum Oxides—From Fundamentals to Functionality. *Adv. Mater.* **2017**, *29*, 1701619. [CrossRef]
2. Yin, H.; Kuwahara, Y.; Mori, K.; Cheng, H.; Wen, M.; Yamashita, H. High-surface-area plasmonic MoO3−x: Rational synthesis and enhanced ammonia borane dehydrogenation activity. *J. Mater. Chem. A* **2017**, *5*, 8946–8953. [CrossRef]
3. Xia, W.; Xu, F.; Zhu, C.; Xin, H.; Xu, Q.; Sun, P.; Sun, L. Sea urchin-like NiCoO2@C nanocomposites for Li-ion batteries and supercapacitors. *Nano Energy* **2016**, *27*, 457–465. [CrossRef]
4. Bessonov, A.; Kirikova, M.; Petukhov, D.; Allen, M.; Ryhänen, T.; Bailey, M. Layered memristive and memcapacitive switches for printable electronics. *Nat. Mater.* **2015**, *14*, 199–204. [CrossRef] [PubMed]
5. Bin, X.; Tian, Y.; Luo, Y.; Sheng, M.; Luo, Y.; Ju, M.; Que, W. High-performance flexible and free-standing N-doped Ti3C2Tx/MoOx films as electrodes for supercapacitors. *Electrochim. Acta* **2021**, *389*, 138774. [CrossRef]
6. Brewer, L.; Lamoreaux, R. The Mo-O system (Molybdenum-Oxygen). *Bull. Alloy Phase Diagr.* **1980**, *1*, 85–89. [CrossRef]
7. Clentsmith, G.; Cloke, F.; Green, J.; Hanks, J.; Hitchcock, P.; Nixon, J. Stabilization of Low-Oxidation-State Early Transition-Metal Complexes Bearing 1,2,4-Triphosphacyclopentadienyl Ligands: Structure of [{Sc(P3C2tBu2)2}2]; ScII or Mixed Oxidation State? *Angew. Chem. Int. Ed. Engl.* **2003**, *42*, 1068–1071. [CrossRef]
8. Scanlon, D.; Watson, G.; Payne, D.; Atkinson, G.; Egdell, R.; Law, D. Theoretical and Experimental Study of the Electronic Structures of MoO_3 and MoO_2. *J. Phys. Chem. C* **2010**, *114*, 4636–4645. [CrossRef]
9. Magnéli, A.; Andersson, G. Studies on the Hexagonal Tungsten Bronzes of Potassium, Rubidium, and Cesium. *Acta Chem. Scand.* **1995**, *9*, 315–324. [CrossRef]
10. Zhao, X.; Cao, M.; Liu, B.; Tian, Y.; Hu, C. Interconnected core–shell MoO_2 microcapsules with nanorod-assembled shells as high-performance lithium-ion battery anodes. *J. Mater. Chem.* **2012**, *22*, 13334–13340. [CrossRef]
11. Shi, Y.; Guo, B.; Corr, S.; Shi, Q.; Hu, Y.; Heier, K.; Chen, L.; Seshadri, R.; Stucky, G. Ordered Mesoporous Metallic MoO_2 Materials with Highly Reversible Lithium Storage Capacity. *Nano Lett.* **2009**, *9*, 4215–4220. [CrossRef]
12. Miyata, N.; Akiyoshi, S. Preparation and electrochromic properties of rf-sputtered molybdenum oxide films. *J. Appl. Phys.* **1985**, *58*, 1651–1655. [CrossRef]
13. Mohamed, S.; Kappertz, O.; Ngaruiya, J.; Leervad Pedersen, T.; Drese, R.; Wuttig, M. Correlation between structure, stress and optical properties in direct current sputtered molybdenum oxide films. *Thin Solid Films* **2003**, *429*, 135–143. [CrossRef]
14. Zhang, W.; Desikan, A.; Oyama, S. Effect of Support in Ethanol Oxidation on Molybdenum Oxide. *J. Phys. Chem.* **1995**, *99*, 14468–14476. [CrossRef]
15. Katrib, A.; Leflaive, P.; Hilaire, L.; Maire, G. Molybdenum based catalysts. I. MoO_2 as the active species in the reforming of hydrocarbons. *Catal. Lett.* **1995**, *38*, 95–99. [CrossRef]
16. Wang, Z.; Zhang, C.; Chen, D.; Tang, S.; Zhang, J.; Wang, Y.; Han, G.; Xu, S.; Hao, Y. Flexible ITO-Free Organic Solar Cells Based on MoO_3/Ag Anodes. *IEEE Photonics J.* **2015**, *7*, 8400109. Available online: https://ieeexplore.ieee.org/document/7021946 (accessed on 1 August 2023).
17. Wang, S.; Guo, H.; Song, Y.; Ma, G.; Li, S.; Zhang, L.; Shao, X. P-63: Lower Reflective TFT Materials and Technology Innovation. *SID Symp. Dig. Tech. Pap.* **2017**, *48*, 1478–1481. [CrossRef]
18. Fernandes Cauduro, A.L.; Fabrim, Z.E.; Ahmadpour, M.; Fichtner, P.F.P.; Hassing, S.; Rubahn, H.-G.; Madsen, M. Tuning the optoelectronic properties of amorphous MoOx films by reactive sputtering. *Appl. Phys. Lett.* **2015**, *106*, 202101. [CrossRef]
19. Liu, Y.; Zhang, H.; Ouyang, P.; Chen, W.; Wang, Y.; Li, Z. High electrochemical performance and phase evolution of magnetron sputtered MoO_2 thin films with hierarchical structure for Li-ion battery electrodes. *J. Mater. Chem. A* **2014**, *2*, 4714–4721. [CrossRef]
20. Qiu, L.; Chen, K.; Yang, D.; Zhang, M.; Hao, X.; Li, W.; Zhang, J.; Wang, W. Metal copper induced the phase transition of MoO_3 to MoO2 thin films for the CdTe solar cells. *Mater. Sci. Semicond.* **2021**, *122*, 105475. [CrossRef]
21. Fujiwara, K.; Tsukazaki, A. Formation of distorted rutile-type NbO_2, MoO_2, and WO_2 films by reactive sputtering. *J. Appl. Phys.* **2019**, *125*, 085301. [CrossRef]
22. Ahn, E.; Lee, J.; Koh, Y.; Lee, J.; Park, B.; Kim, J.; Lee, I.; Lee, C.; Jeen, H. Low Temperature Nanoscale Oxygen-Ion Intercalation into Epitaxial MoO_2 Thin Films. *J. Phys. Chem. C* **2017**, *121*, 3410–3415. [CrossRef]
23. Martínez, M.A.; Guillén, C. Comparison between large area dc-magnetron sputtered and e-beam evaporated molybdenum as thin film electrical contacts. *J. Mater. Process. Technol.* **2003**, *143–144*, 326–331. [CrossRef]
24. Pachlhofer, J.; Martín-Luengo, A.; Franz, R.; Franzke, E.; Köstenbauer, H.; Winkler, J.; Bonanni, A.; Mitterer, C. Industrial-scale sputter deposition of molybdenum oxide thin films: Microstructure evolution and properties. *J. Vac. Sci. Technol. A* **2017**, *35*, 021504. [CrossRef]
25. Park, H.; Ryu, J.; Youn, H.; Yang, J.; Oh, I. Fabrication and Property Evaluation of Mo Compacts for Sputtering Target Application by Spark Plasma Sintering Process. *Mater. Trans.* **2012**, *53*, 1056–1061. [CrossRef]
26. Durnez, A.; Petitbon-Thévenet, W.; Fortuna, F.; Radioanal, J. Preparation of molybdenum target by centrifugal method. *J. Radioanal. Nucl. Chem.* **2014**, *299*, 1149–1154. [CrossRef]
27. Wang, Y.; Tang, Q.; Chen, D.; Liu, X.; Xiong, X. Microstructure and Magnetron Sputtering Properties of Molybdenum Target Prepared by Low-Pressure Plasma Spraying. *J. Therm Spray Technol.* **2019**, *28*, 1983–1994. [CrossRef]
28. Kitchamsetti, N.; Choudhary, R.; Phase, D.; Devan, R. Structural correlation of a nanoparticle-embedded mesoporous $CoTiO_3$ perovskite for an efficient electrochemical supercapacitor. *RSC Adv.* **2020**, *10*, 23446. [CrossRef]

29. Ganapathi, S.; Owen, D.; Chokshi, A. The kinetics of grain growth in nanocrystalline copper. *Scr. Metall. Mater.* **1991**, *25*, 2699–2704. [CrossRef]
30. Adrian, A.B.; Brendan, J.K.; Christopher, J.H. Neutron Powder Diffraction Study of Molybdenum and Tungsten Dioxides. *Aust. J. Chem.* **1995**, *48*, 1473–1477. [CrossRef]
31. Jacob, K.; Saji, V.; Gopalakrishnan, J.; Waseda, Y. Thermodynamic evidence for phase transition in MoO_{2-d}. *J. Chem. Thermodyn.* **2007**, *39*, 1539–1545. [CrossRef]
32. Wakai, F.; Yoshida, M.; Shinoda, Y.; Akatsu, T. Coarsening and grain growth in sintering of two particles of different sizes. *Acta Metall.* **2005**, *53*, 1361–1371. [CrossRef]
33. Scherrer, P. Bestimmung der Grosse und inneren Struktur von Kolloidteilchen mittels Rontgenstrahlen. *Nach. Ges. Wiss. Gottingen.* **1918**, *2*, 98–100.
34. Holzwarth, U.; Gibson, N. The Scherrer equation versus the 'Debye-Scherrer equation'. *Nat. Nanotechnol.* **2011**, *6*, 534. [CrossRef] [PubMed]
35. Klug, H.; Alexander, L. *X-ray Diffraction Procedures: For Polycrystalline and Amorphous Materials*, 2nd ed.; Wiley: Hoboken, NJ, USA, 1974. Available online: https://ui.adsabs.harvard.edu/abs/1974xdpf.book.....K/abstract (accessed on 1 August 2023).
36. Dos Reis, M.; Giret, Y.; Carrez, P.; Cordier, P. Efficiency of the vacancy pipe diffusion along an edge dislocation in MgO. *Comput. Mater. Sci.* **2022**, *211*, 111490. [CrossRef]
37. Burke, J.; Turnbull, D. Recrystallization and grain growth. *Prog. Phys. Met.* **1952**, *3*, 275–292. [CrossRef]
38. Wang, F. *Ceramic Fabrication Processes: Treatise on Materials Science and Technology*; Academic Press Inc.: Orlando, FL, USA, 1976; Volume 9. Available online: https://books.google.co.kr/books?hl=en&lr=&id=00MvBQAAQBAJ&oi=fnd&pg=PP1&ots=-hofU5QfJ6&sig=MtR1oCG1XwI-BY5xhn7jhpW39ZA&redir_esc=y#v=onepage&q&f=false (accessed on 1 August 2023).
39. Lu, K. Nanocrystalline metals crystallized from amorphous solids: Nanocrystallization, structure, and properties. *Mater. Sci. Eng. R.* **1996**, *16*, 161–221. [CrossRef]